

Optimizing Photovoltaic Charge Generation of Nanowire Arrays: A Simple Semi-Analytic Approach

Björn C. P. Sturmberg,^{*,†} Kokou B. Dossou,[‡] Lindsay C. Botten,[‡] Ara A. Asatryan,[‡] Christopher G. Poulton,[‡] Ross C. McPhedran,[†] and C. Martijn de Sterke[†]

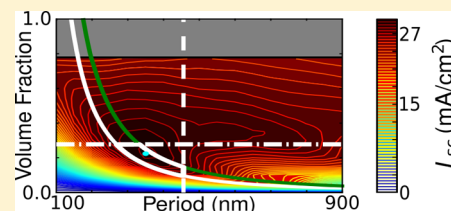
[†]CUDOS and IPOS, School of Physics, University of Sydney, Sydney, 2006, Australia

[‡]CUDOS, School of Mathematical Sciences, University of Technology Sydney, Sydney, 2007, Australia

S Supporting Information

ABSTRACT: Nanowire arrays exhibit efficient light coupling and strong light trapping, making them well suited to solar cell applications. The processes that contribute to their absorption are interrelated and highly dispersive, so the only current method of optimizing the absorption is by intensive numerical calculations. We present an efficient alternative that depends solely on the wavelength-dependent refractive indices of the constituent materials. We choose each array parameter such that the number of modes propagating away from the absorber is minimized, while the number of resonant modes within the absorber is maximized. From this we develop a semi-analytic method that quantitatively identifies the small range of parameters where arrays achieve maximum short-circuit currents. This provides a fast route to optimizing NW array cell efficiencies by greatly reducing the geometries to study with full device models. Our approach is general and applies to a variety of materials and to a large range of array thicknesses.

KEYWORDS: photovoltaics, solar energy, nanowire arrays, light trapping, nanophotonics, diffraction gratings



A major challenge in solar energy research is to reduce the cost-per-watt of photovoltaic cells. This challenge may be met by increasing the efficiency, as in the case of multijunction cells,¹ or by reducing costs through the use of less expensive materials.^{2,3} The cost-per-watt can also be reduced by using established materials in much thinner films than standard cells.^{4,5} This last approach greatly reduces costs, but also reduces the efficiency if the cell design is not modified. The efficiency decrease is largely due to optical losses, not only from increased transmission due to incomplete absorption, but also from increased reflection at the front surface, which can no longer be coated with standard multiple micrometer-thick antireflective patterns. Structuring the thin absorbing layer into vertically aligned nanowire (NW) arrays has been shown to address both these losses simultaneously, by increasing the *light coupling* into the cell and enhancing the absorption through *light trapping*. Further advantages of NWs include compatibility with cheap flexible substrates⁶ and radial p–n junctions.^{7–9} NWs also reduce the lattice matching constraints that limit material combinations in multijunction devices.¹⁰ These structures have therefore attracted intense theoretical^{11–14} and experimental^{16,15–20} research, with efficiencies of 13.8% being reported.²¹

Optimizing the photovoltaic performance of NW arrays is challenging because their optical and electronic properties depend strongly upon the arrays' geometry. Typically, simulations are first carried out to assess the optical charge carrier generation, and then the charge carrier collection performance is calculated separately. Recently, techniques for combined optoelectronic modeling of nanostructured photo-

voltaics have been developed that recursively calculate the generation, collection, and recombination of charge carriers.²² All of these numerical approaches are limited to grid searches of small parts of parameter space, wherein they locate local optima. Finding a general optimum, or fully understanding the behavior of NW arrays using such means, is however impracticable due to the range of parameters. In particular, the high sensitivity of the charge carrier profile to experimental factors such as material quality, fabrication techniques, passivation method, and device design prohibits the carrier collection efficiency from being incorporated into a general optimization routine. These issues also limit the predictive information that can be gained from experiments. For example, the fill factors of current state of the art III–V NW array solar cell vary between 25% and 77%.²³ It is therefore valuable to fully understand the charge generation aspects of NW arrays before modeling their charge collection. A compromise between maximal charge generation and efficient charge collection can then be found to maximize the photovoltaic energy conversion efficiency.

The charge generation of NW arrays is directly related to their optical absorption,²⁴ which is less dependent on material processing. The absorption in turn however is driven by numerous competing optical effects, including the excitation of guided resonance modes and higher diffraction orders.^{11–14} Since these are resonant effects, they are highly dispersive

Received: March 24, 2014

Published: July 1, 2014

across the broad bandwidth of the solar spectrum, and it is unclear how to best balance their effects to maximize the total absorption. This is made more difficult by each wavelength contributing an amount given by the solar spectrum. These factors all combine to produce a challenging optimization problem that is currently addressed by fully numerical studies of specific sections of parameter space.^{12,13,16,18}

SEMI-ANALYTIC APPROACH

Here we present an approach that allows the optimal design parameters for maximal charge generation to be evaluated semi-analytically in negligible time for a given material and thickness. This provides an ideal starting point for numerical and experimental studies of the electrical performance of NW geometries. We do this by constructing an integrated theoretical framework that relates the reflection, transmission, and absorption of NW arrays to their geometric parameters (Figure 1): radius a , period d , thickness h , and volume fraction

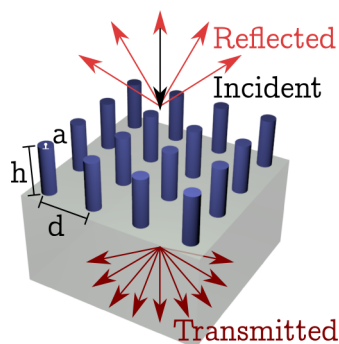


Figure 1. Geometry of vertically aligned nanowire arrays showing light incident normally and diffracted into the zeroth and higher orders in reflection and transmission. While our optimization method is independent of lattice type, numeric simulations use a square lattice as shown.

f . In our numerical calculations we consider square lattices for which $f = \pi \times a^2/d^2$; however studies have reported a weak influence of lattice type on the absorption of NW arrays,^{13,25} and our analytic model is independent of the lattice type. From these relationships we develop a simple method that quantitatively identifies the small region of optimal parameter space for charge generation.

For each choice of material system and thickness we analyze the parameter space presented in Figure 2. Here the period and volume fraction are indicated on the axes, and curves of constant radius are of the form $f \propto 1/d^2$. Arrays whose NWs intersect are excluded by the gray region, which for square arrays is $f > \pi/4$. The colored contours of Figure 2 indicate numerically calculated short-circuit currents, J_{sc} , of NW arrays where the array that produces maximal J_{sc} is marked with a blue dot. Overlaid on the numerical results, with white and green curves, are the predictions of our semi-analytic optimization. Briefly this optimization method is described as dividing parameter space into regions that have either too high a reflectance (above the horizontal dot-dashed line) or too much transmission (right of the vertical dashed line) or do not support enough resonant absorption modes (outside of the region between the white and green curves). The optimal NW design must therefore lie within the region highlighted in thick white curves. The considerations dictating these reductions make use of the coupled wave argument developed by Yu et

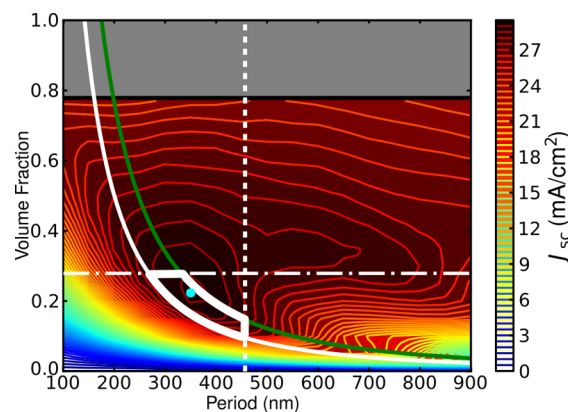


Figure 2. Numerically calculated short-circuit current of InP NW arrays across the parameter space $100 \text{ nm} < d < 900 \text{ nm}$, $0.005 < f < 0.780$. The optimal array is marked with a blue dot and has $J_{sc} = 29.2 \text{ mA/cm}^2$. Superimposed are the results of our semi-analytic optimization with the predicted optimal region emphasized with thick curves.

al.²⁶ That is, the absorption is highest when the number of outward propagating modes is minimized, while the number of resonant modes within the absorbing layer is simultaneously maximized. Here we extend this approach by considering the modal amplitudes and by integrating across the solar spectrum to calculate parameter constraints in terms of the maximum short-circuit current.

We illustrate our method using InP NWs surrounded by an air background ($n = 1$), placed upon a semi-infinite SiO_2 substrate under an air superstrate. We stress however that the method applies to a wide variety of materials including direct and indirect band gap semiconductors. Results for GaAs, silicon, and germanium are contained in the Supporting Information. We first examine the effect of radius, period, and volume fraction while fixing $h = 2.33 \mu\text{m}$ and thereafter show that the thickness determines the relative importance of reflection versus transmission losses. Our semi-analytic predictions show excellent agreement for the optimal array parameters when compared to full simulations.

Effect of NW Radius on Absorption Resonances. We begin by studying the role of the NW radius. It has been shown that NW arrays support guided resonance modes, each of which drive strong absorption peaks. These modes have been described in the literature as either leaky optical fiber modes^{14,27} or as Key (Bloch) Modes (KMs).¹¹ These descriptions are equivalent for sparse arrays, where the NW surfaces are far apart, but differ for dense arrays, where the effect of the lattice, which is included only in the Bloch mode formulation, becomes significant (see Supporting Information for derivation of equivalence in the sparse limit). Though here we consider perfectly cylindrical NWs, the lower order modes of NWs depend on the cross-sectional area so that minor perturbations in shape do not alter the dipolar nature of the fields, and for our purposes here the same equations can be applied. A fundamental property of waveguides is that the number of bound modes increases with the dimension of the cross-section. Applied to NWs this means that the number of KMs grows with increasing radius. This suggests a clear optimization goal; choose the NW radius as large as possible, so as to maximize the number of absorption resonances.

However, absorption resonances contribute to the absorption of the solar cell only if they occur at wavelengths where the

material absorbs and where there is incoming solar radiation. This is the range $\lambda_1 < \lambda < \lambda_g$, where $\lambda_1 = 310$ nm is the lower limit of the solar spectrum and λ_g is the band gap wavelength of the absorbing material, which for InP is $\lambda_g = 922.5$ nm. It is known that the symmetry of the incident light allows only HE_{1m} fiber modes to be effectively excited.^{14,28} We have found that the strongest excitations occur at frequencies slightly above the $\text{Re}(\beta_z) = 0$ cutoff of these modes, where β_z is the propagation constant of the mode. Hence, the strongest absorption occurs when

$$\frac{\varepsilon_1 J_1'(k_1 a)}{k_1 J_1(k_1 a)} - \frac{\varepsilon_2 H_1^{(1)'}(k_2 a)}{k_2 H_1^{(1)}(k_2 a)} = 0 \quad (1)$$

which can be derived from the standard transcendental equation for HE modes in the limit $\beta \rightarrow 0$. Here ε_i and $k_i = (\varepsilon_i \omega^2 / c^2 - \beta_z^2)^{1/2}$ are the permittivities and transverse wavenumbers in the NWs ($i = 1$) and background ($i = 2$), respectively, J_1 is the first-order Bessel function, and $H_1^{(1)}$ is the first-order Hankel function of the first kind. Incidentally, this expression is identical to the one obtained for the key modes, the Bloch modes that are known to dominate the absorption in NW arrays, in the limit in which the lattice period becomes arbitrarily large (i.e., as $S_0 \rightarrow 0$ in eq 10 in Sturmburg et al.¹¹). The fundamental HE_{11} fiber mode does not have a cutoff. It therefore exists for all radii at all wavelengths, but does not contribute a large absorption peak and is not counted in Figure 3a. For the derivation of eq 1 and the relationship between KMs and HE_{1m} fiber modes see the Supporting Information.

Using eq 1 we scan through possible NW radii, recording when key modes enter and leave the spectrum: $\text{Re}(\beta_z(\lambda_1)) = 0$, $\text{Re}(\beta_z(\lambda_g)) = 0$, respectively. These radii are represented in Figure 3a as black curves where an additional mode enters the

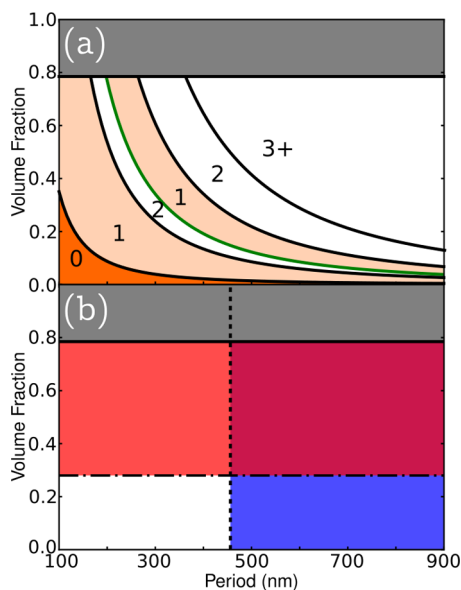


Figure 3. (a) NW array parameter space showing the NW radii at which KMs enter (black curves) and leave (red curve) the absorption spectrum. The number of KMs within the absorption spectrum is shown for each region, where darker shades of orange indicate fewer KMs. (b) Constraints placed on the optimal region of parameter space due to high transmission (blue area) and high reflection (red area). The region of high transmission and reflection is colored magenta. Optimal NW array geometries lie in the union of the white regions of (a) and (b).

spectrum and as green curves where a mode leaves the spectrum. Between the curves the number of KMs is constant, as labeled in Figure 3a. From this analysis we require the optimal arrays to be in one of the regions with at least two KMs, such as immediately to the left of the green curve or toward the top right of the figure. There is a preference for small radii because the fields of higher order modes, which are supported by larger NWs, have a greater number of nodes within the NW and therefore couple less well to the incident plane waves. For diagrammatic purposes we include only the first three KMs in Figure 3a.

Having identified the light-trapping advantages of larger NWs, we now consider two processes that impose upper limits to the optimal NW radius. These arise because the NWs are arranged in a periodic lattice; thus, increasing the radius we can either keep the volume fraction constant and adjust the period or keep the period constant and adjust the volume fraction. These correspond, respectively, to moving horizontally and vertically through Figure 2. In each case we observe that the absorption initially grows with increasing radius, but eventually decreases. It is by uncovering the origins of this behavior that we can define the vertical and horizontal restrictions shown in Figure 2.

Effect of Array Period on Transmission Channels. We investigate the role of increased period in Figure 4, where we

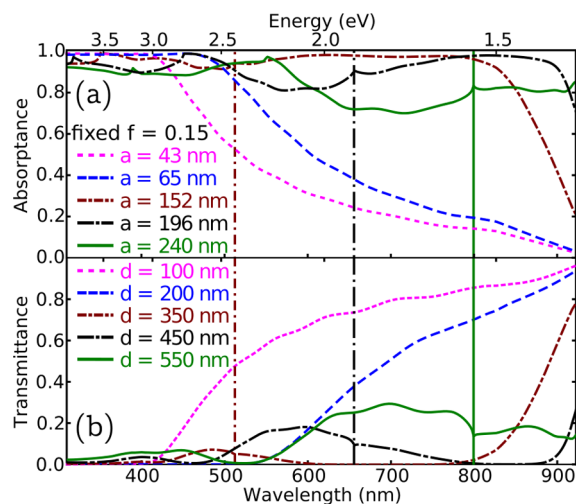


Figure 4. Absorption (a) and transmission (b) spectra as NW radius is increased with a fixed volume fraction $f = 0.15$. Vertical lines mark the shortest wavelength Wood anomalies in the substrate $\lambda_{\text{WA}} = n_{\text{sub}} d$.

show the absorption and transmission spectra of InP arrays with radii in the range 43–240 nm and fixed volume fraction $f = 0.15$, i.e., moving horizontally in Figure 2. In Figure 4a the absorption initially increases with radius, but once $a > 152$ nm ($d > 350$ nm), the absorption of long wavelengths is significantly reduced. It is clear from Figure 4b that this decrease is due to a rise in transmission, while the reflectance is relatively constant for all arrays, with $R < 7\%$ across the spectrum (see Supporting Information). The increase in transmission is caused by the periodically varying refractive index of the NW array exciting nonzero diffraction orders in the substrate, which increases the number of channels propagating energy away from the array from 1 to 5 for wavelengths below the zero-order Wood anomaly. This anomaly occurs at $\lambda = \lambda_{\text{WA}}$, which is indicated in Figure 4 by vertical lines in the line style of

the corresponding spectrum. In transmission the shortest wavelength Wood anomaly occurs at $\lambda_{\text{WA}} = n_{\text{sub}}d$, where n_{sub} is the refractive index of the substrate. For $\lambda > \lambda_{\text{WA}}$ all nonzero diffraction orders are evanescent and, as such, do not contribute to the energy flow. The excitation of higher diffraction orders therefore adds a qualifier to the optimization; incorporate large NW radii, but do so while imposing an upper limit on the period.

The strictest limit to place on the period is that no higher diffraction orders are allowed to exist within the solar spectrum, which limits the period to $d < 310 \text{ nm}/n_{\text{sub}} = 213 \text{ nm}$ for a SiO_2 substrate. This criterion however fails to consider the strong absorption of short wavelengths that do not reach the substrate, which renders the number of transmission channels irrelevant for these wavelengths. We must therefore choose a longer wavelength λ_{av} from which we can derive the maximum allowable period, $d_{\text{max}} \equiv \lambda_{\text{av}}/n_{\text{sub}}$.

Our approach is to choose λ_{av} to be an averaged wavelength, on the short wavelength side of which the nonzero transmission channels can be tolerated, while there is only a single transmission channel at longer wavelengths. To account for the highly nonuniform spectral intensity of the solar spectrum, we weight each above-band-gap wavelength by the number of solar photons incident at that wavelength, $\xi(\lambda) = I(\lambda)\lambda/hc$, where $I(\lambda)$ is the irradiance as given in the ASTM air mass 1.5 spectrum,²⁹ h is Planck's constant, and c is the speed of light in a vacuum:

$$\lambda_{\text{av}} = \frac{\int_{\lambda_1}^{\lambda_2} \xi(\lambda) \lambda \, d\lambda}{\int_{\lambda_1}^{\lambda_2} \xi(\lambda) \, d\lambda} \quad (2)$$

For InP this gives $\lambda_{\text{av}} = 665 \text{ nm}$. We take an analogous weighted average of the substrate refractive index, replacing λ in the numerator with $n(\lambda)$, which gives $n_{\text{sub}} = 1.46$. The maximum allowed period is therefore $d_{\text{max}} = 456 \text{ nm}$, which is represented in Figure 3b by the start of the blue region.

Effect of Volume Fraction on Reflectance. Having examined the effect of increasing NW radii within lattices of increasing periods (i.e., moving horizontally in Figure 2), we now move vertically through Figure 2. Figure 5 shows the

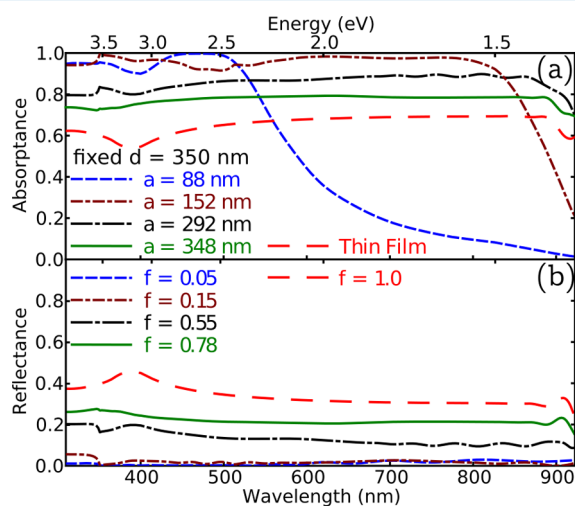


Figure 5. Absorption (a) and reflection (b) spectra as NW radius is increased with a period $d = 350 \text{ nm}$. The spectra of a homogeneous film of equal thickness are shown in red ($f = 1.0$).

absorption and reflection spectra for arrays with fixed period $d = 350 \text{ nm}$ and radii increasing from $a = 88 \text{ nm}$ to $a = 348 \text{ nm}$ ($0.05 \leq f \leq 0.78$). The spectra of a homogeneous film of equal thickness ($f = 1.0$) are also shown to emphasize the excellent antireflective light coupling performance of the NW arrays. The transmittance of these arrays, shown in the Supporting Information, is relatively constant once $f \geq 0.55$. In contrast to Figure 4a, the absorption in Figure 5a decreases uniformly across the spectrum once $a > 152 \text{ nm}$ and does so due to a uniform increase in reflectance. The Wood anomaly in reflection that occurs at $\lambda_{\text{WA}} = n_{\text{Airy}}d = 350 \text{ nm}$ produces only a minor enhancement in short wavelength reflection, which is unaffected by the increase in f (since d is constant). The increased reflectance is therefore due not to a larger number of reflected propagating orders but to a larger amplitude of the zeroth reflection order. This trend is not surprising: as the InP volume fraction increases, so does the average refractive index, and therefore so does the Fresnel reflection.

To incorporate the influence of Fresnel reflections on the optimization, we determine an upper bound on the volume fraction, f_{max} , that does not impede the integrated absorption. This is a subtle procedure that depends on the thickness of the absorbing layer: thick layers can be expected to absorb most of the light that enters, and minimizing reflection is therefore paramount. In contrast, thin layers with limited absorption can tolerate more reflection if it leads to higher absorption. Rather than dealing with the absorption, we use the transmission as a proxy since, for example, thick layers with strong absorption have little transmission. We therefore define the largest volume fraction allowed as that for which the average reflection equals the average transmission. The reflectance $R(\lambda)$ and transmittance $T(\lambda)$ are estimated using the Fresnel equations with the NW array replaced by a thin film of equal thickness composed of an effective medium with permittivity $\epsilon_{\text{eff}}(f, \lambda)$. The critical volume fraction f_{max} is then defined as the f such that $R_{\text{av}}(\epsilon_{\text{eff}}(f)) = T_{\text{av}}(\epsilon_{\text{eff}}(f))$, where the average reflectance and transmittance are calculated as in eq 3 (see Supporting Information for derivation). For InP NW arrays with $h = 2.33 \mu\text{m}$, $f_{\text{max}} = 0.28$, which is indicated in Figure 3b by the red shading of $f > 0.28$.

$$R_{\text{av}}(f) = \frac{\int_{\lambda_1}^{\lambda_2} \xi(\lambda) R(f, \lambda) \, d\lambda}{\int_{\lambda_1}^{\lambda_2} \xi(\lambda) \, d\lambda} \quad (3)$$

It is important to note that this limit relies on the calculation of effective indices for structures that include significant loss. Existing effective index models, such as Maxwell–Garnett, poorly approximate the complex effective indices for these structures. It has recently been proposed in studies on mesoporous thin films that the real and imaginary components of the effective indices of lossy structures may be best calculated independently from different effective index formulations. As in these studies,^{30,31} we found such an approach to best replicate the observed reflectance and transmission spectra and subsequently to most reliably predict f_{max} . We calculate $\text{Re}(\epsilon_{\text{eff}})$ using the Bruggeman formulation³² and $\text{Im}(\epsilon_{\text{eff}})$ using the volume averaging theory.^{33,34}

■ COMPARISON TO NUMERIC SIMULATIONS

To make a final prediction of the optimal array parameters, we combine the three arguments developed above. This corresponds to placing the restrictions on period and volume

fraction of Figure 3b onto the radius goals of Figure 3a. In doing so, we remove the top right region of parameter space that supports three KMs, as well as the slightly smaller radius region that supports two KMs. The optimal region is therefore predicted to be just to the left of the green curve, where two KMs are supported without the excitation of too many transmission channels or too high a top surface reflectance. To verify this prediction, we calculate the short-circuit current J_{sc} of InP NW arrays across the parameter space of $100 \text{ nm} < d < 900 \text{ nm}$, $0.005 < f < 0.780$ with $h = 2.33 \mu\text{m}$. We sampled this parameter space with 993 simulations.

Figure 2 shows these numerical results as well as the semi-analytic predictions for f_{max} , d_{max} and the radius limits within which two KMs are supported. The agreement is excellent, with the optimal arrays located under f_{max} to the left of d_{max} and above the white solid curve ($a = 80 \text{ nm}$) that indicates the presence of the second KM resonance within the absorption range. The optimal array was found to have a period of $d = 350 \text{ nm}$ and a volume fraction of $f = 0.22$ and had a short-circuit current of $J_{sc} = 29.2 \text{ mA/cm}^2$. The optimum array is marked with a blue dot and is located to the left of the green curve ($a = 99 \text{ nm}$), where the first KM leaves the absorption range. The near-optimal arrays that are in close proximity to the green curve, but on its right side, arise because these arrays still have a large fraction of the KM resonant absorption peak within the absorption range. The contours of other regions also substantiate our approach; the horizontal contours above the f_{max} line indicate a volume fraction dominated (period-independent) decrease in absorption, while the parameter space with small f and large d exhibits near vertical contours, demonstrating the strong influence of period here.

Dependence on Array Thickness. The above analysis has been limited to arrays of fixed thickness, with the comparison in Figure 2 being for $h = 2.33 \mu\text{m}$. It is however straightforward to extend the approach to other thicknesses, requiring only f_{max} to be re-evaluated, due to the dependence of $T(\varepsilon_{\text{eff}}(f))$ on the array thickness. In Figure 6 we show the semi-analytic predictions for arrays of (a) $h = 1.5 \mu\text{m}$ and (b) $h = 4 \mu\text{m}$ along with the corresponding numerical calculations for J_{sc} . The predictions continue to agree well with the numerical results, as the optimum shifts to lower f with increased h . This is well approximated by the balancing of transmission versus reflection through the effective medium, as demonstrated from the semi-analytic horizontal lines.

Comparing our calculated short-circuit currents to the best reported experimental results, we find that for $h = 1.5 \mu\text{m}$ our maximum J_{sc} of 28.2 mA/cm^2 is 4.2 mA/cm^2 greater than that reported by Wallentin et al.²¹ for InP NWs of equal thickness. While some of this difference is accounted for by the absence of carrier losses in our optical simulations, the J_{sc} we calculate for the geometry they fabricated is only 1.3 mA/cm^2 greater than their experimentally measured value. This leaves almost 3 mA/cm^2 to be gained by optical optimization. The geometry of Wallentin et al. would gain this improvement by doubling the volume fraction from 0.12 to 0.25, while keeping the radius of the NWs at the already optimal 180 nm .

We chose a thickness of $h = 4 \mu\text{m}$ in Figure 6b because this is the thickness of the record efficiency planar InP solar cell.^{35,36} This planar cell has $J = 29.5 \text{ mA/cm}^2$, while the optimal NW array ($d = 400 \text{ nm}$, $f = 0.17$) has $J_{sc} = 29.9 \text{ mA/cm}^2$. This would suggest that, at this thickness, a planar structure is superior to a NW array once carrier losses are included in fabricated NW arrays. However, the record planar cell contains an antireflective

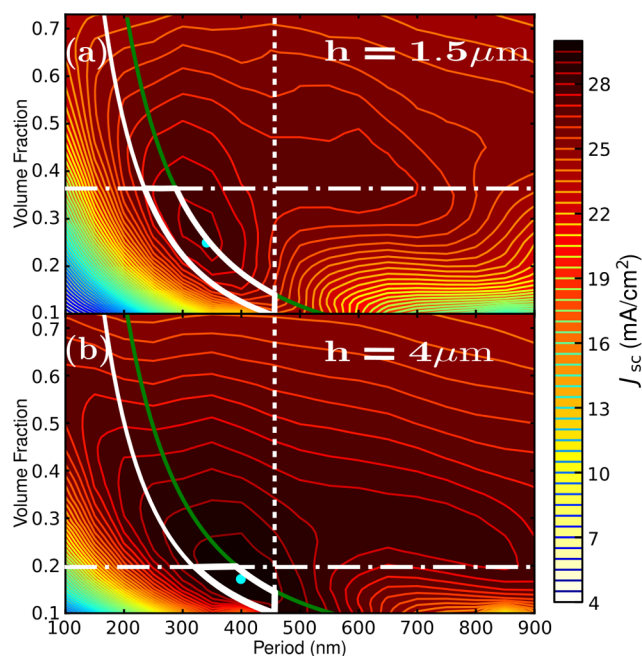


Figure 6. Numerically calculated short-circuit currents J_{sc} of InP NW arrays of height (a) $h = 1.5 \mu\text{m}$ and (b) $h = 4 \mu\text{m}$. The optimal arrays are marked with blue dots and have (a) $J_{sc} = 28.2 \text{ mA/cm}^2$ and (b) $J_{sc} = 29.9 \text{ mA/cm}^2$. Superimposed are the results of our semi-analytic optimization with the predicted optimal region emphasized with thick curves.

coating and a Zn–Au back reflector, neither of which are present in our NW simulations. Given the NW arrays' excellent antireflection properties, we do not introduce an antireflective layer; however when we include an Au back reflector, the NW arrays obtain $J_{sc} = 30.5 \text{ mA/cm}^2$ for thicknesses of $4 \mu\text{m}$. Consistent with our semi-analytic optimization the optimal arrays that included back reflectors have larger periods because there are no longer any diffraction orders excited in the substrate. The only waves that carry energy away from the NWs are in the air superstrate such that $d_{\text{max}} = \lambda_{\text{av}}/n_{\text{air}}$. These results suggest that it may be possible for NW arrays to outperform even the record planar cell that consumes 10 times the amount of InP.

We note that the results of Figure 6 were calculated simultaneously along with 49 other heights across the range $1\text{--}50 \mu\text{m}$. This was done with negligibly increased computational expense by virtue of the generalized scattering matrix method³⁷ as implemented in the freely available EMUstack simulation package.³⁸ For all thicknesses in this range the numerically calculated optima lie within the region predicted by our optimization method.

CONCLUSION

We have constructed a simple optimization method to maximize the photovoltaic charge generation of NW arrays. Our method depends solely on the refractive indices of the constituent materials and can be evaluated essentially instantaneously, providing a refined starting point for device modeling of NW array solar cells. The physical premise of our approach is to maximize the light trapping of the structure while simultaneously enhancing the light coupling into the solar cell. To achieve optimal light trapping, we showed that the NW radius should be increased so as to support more resonant

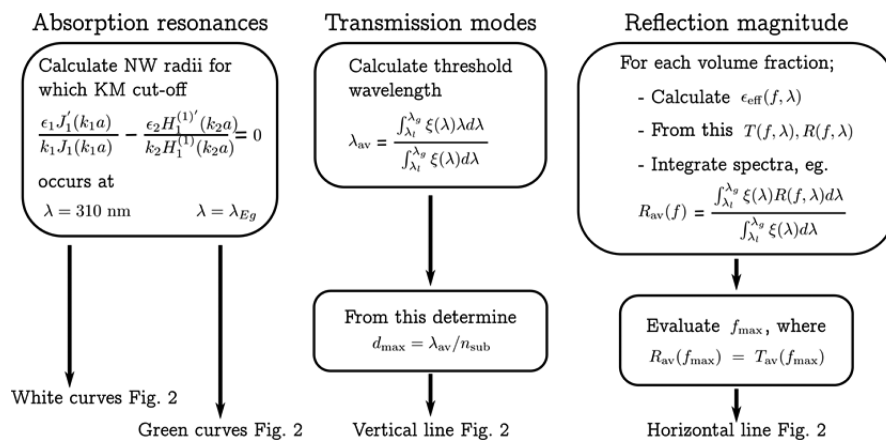


Figure 7. Flowchart outlining our semi-analytic optimization procedure. The number of resonant modes within the spectrum is found by first calculating where additional key modes enter the absorption range (plotted as white curves) and then calculating where they leave this range (green curves). Next, the upper bound on the period is determined and marked with a vertical line. The optimal region is then enclosed by the horizontal line, which limits the acceptable volume fraction of the array above which the reflection is too great.

modes and the period should remain less than d_{max} to limit the number of outwardly propagating plane waves excited. Meanwhile to enhance the light coupling into the array, the volume fraction must be restricted to $f < f_{max}$. From this simple ansatz we developed expressions that quantitatively define the region of parameter space where NW arrays have optimal J_{sc} .

Figure 7 outlines our optimization method, summarizing the equations that quantify the limits of the optimal parameter space. By following this procedure the NW array geometries that maximize charge generation can be rapidly identified, guiding further electronic modeling and experimental investigations to simultaneously optimize the charge collection efficiency.

The construction of these arguments requires a fine balance between making simplifying approximations and retaining the essential physics of the various optical effects. In the calculation of f_{max} for example, the essential physics of balancing reflection losses against transmission losses was accentuated, while all other effects, such as the modes of the NWs, were omitted through the use of an effective index treatment. Similarly, the derivation of d_{max} was based on a simple physical argument about the excitation of diffraction orders, but required the considered selection of a critical wavelength λ_{av} . Although the analysis presented here is restricted to normal incidence, it is straightforward to generalize the expressions to off-normal incidence, and we note that previous studies of NW arrays have found that the integrated absorption of NW arrays is altered little for non-normal angles of incidence up to 40° .^{11,12}

The results contained in the Supporting Information for GaAs, silicon, and germanium NW arrays show that the presented analytic optimization is robust to the very different refractive indices of these materials, including large dispersive variations in absorption coefficients. These differences produce distinct semi-analytic predictions and unique J_{sc} contour topologies. For example, silicon arrays of thickness $h = 2.33 \mu\text{m}$ have an optimal volume fraction of $f = 0.7$ due to silicon's low absorptivity and an optimal period of $d = 500 \text{ nm}$ due to its larger band gap.

■ ASSOCIATED CONTENT

Supporting Information

Supporting Information contains comparisons of our semi-analytic optimization to numerically calculated values of J_{sc} for

silicon, germanium, and GaAs NW array solar cells. It also contains the reflection and transmission spectra complementing Figures 4 and 5, the derivation of the dispersion relation of KMs and HE_{1m} fiber modes that lead to eq 1, and the derivation of f_{max} . This material is available free of charge via the Internet at <http://pubs.acs.org>.

■ AUTHOR INFORMATION

Corresponding Author

*E-mail: b.sturmburg@physics.usyd.edu.au.

Notes

The authors declare no competing financial interest.

■ ACKNOWLEDGMENTS

This work was supported by the Australian Renewable Energy Agency and the Australian Research Council Discovery Grant and Centre of Excellence Schemes. Computation resources were provided by the National Computational Infrastructure, Australia. We acknowledge useful discussions with Dr. T. White and Dr. K. Catchpole.

■ REFERENCES

- (1) King, R. R.; Boca, A.; Hong, W.; Liu, X.; Bhusari, D.; Larrabee, D.; Edmondson, K. M.; Law, D. C.; Fetzer, C. M.; Mesropian, S.; Karam, N. H. Band-gap-engineered architectures for high-efficiency multijunction concentrator solar cells. *Conf. Rec., 24th Eur. Photovoltaic Sol. Energy Conf.* **2009**, 21–25.
- (2) Todorov, T. K.; Reuter, K. B.; Mitzi, D. B. High-efficiency solar cell with earth-abundant liquid-processed absorber. *Adv. Mater.* **2010**, *22*, E156–159.
- (3) Liu, M.; Johnston, M. B.; Snaith, H. J. Efficient planar heterojunction perovskite solar cells by vapour deposition. *Nature* **2013**, *501*, 395–398.
- (4) Catchpole, K. R. Nanostructures in photovoltaics. *Philos. Trans. R. Soc. A* **2006**, *364*, 3493–3503.
- (5) Tsakalagos, L. Nanostructures for photovoltaics. *Mater. Sci. Eng. R* **2008**, *62*, 175–189.
- (6) Fan, Z.; Razavi, H.; Do, J.-w.; Moriwaki, A.; Ergen, O.; Chueh, Y.-L.; Leu, P. W.; Ho, J. C.; Takahashi, T.; Reichertz, L. A.; Neale, S.; Yu, K.; Wu, M.; Ager, J. W.; Javey, A. Three-dimensional nanopillar-array photovoltaics on low-cost and flexible substrates. *Nat. Mater.* **2009**, *8*, 648–653.
- (7) Kayes, B. M.; Filler, M. A.; Henry, M. D.; Maiolo, J. R., III; Kelzenberg, M. D.; Putnam, M. C.; Spurgeon, J. M.; Plass, K. E.;

Scherer, A.; Lewis, N. S.; Atwater, H. A. Radial p-n junction, wire array solar cells. *33rd IEEE Photovoltaic Spec. Conf.* **2008**, 1–5.

(8) Garnett, E. C.; Yang, P. Silicon nanowire radial p-n junction solar cells. *J. Am. Chem. Soc.* **2008**, *130*, 9224–9225.

(9) Mariani, G.; Scofield, A. C.; Hung, C.-H.; Huffaker, D. L. GaAs nanopillar-array solar cells employing in situ surface passivation. *Nat. Commun.* **2013**, *4*, 1497.

(10) Endo, H.; Goto, H.; Maebashi, T.; Nishijima, M.; Nakamura, N. Multi-junction solar cell and manufacturing method therefor. U.S. Patent 0327384, 2013.

(11) Sturmberg, B. C. P.; Dossou, K. B.; Botten, L. C.; Asatryan, A. A.; Poulton, C. G.; de Sterke, C. M.; McPhedran, R. C. Modal analysis of enhanced absorption in silicon nanowire arrays. *Opt. Express* **2011**, *19*, A1067–1081.

(12) Lin, C.; Povinelli, M. L. Optical absorption enhancement in silicon nanowire arrays with a large lattice constant for photovoltaic applications. *Opt. Express* **2009**, *17*, 19371–19381.

(13) Alaeian, H.; Atre, A. C.; Dionne, J. A. Optimized light absorption in Si wire array solar cells. *J. Opt.* **2012**, *14*, 024006.

(14) Wang, B.; Leu, P. W. Tunable and selective resonant absorption in vertical nanowires. *Opt. Lett.* **2012**, *37*, 3756–3758.

(15) Gunawan, O.; Wang, K.; Fallahzad, B.; Zhang, Y.; Tutuc, E.; Guha, S. High performance wire-array silicon solar cells. *Prog. Photovolt. Res. Appl.* **2010**, *19*, 307–312.

(16) Hu, L.; Chen, G. Analysis of optical absorption in silicon nanowire arrays for photovoltaic applications. *Nano Lett.* **2007**, *7*, 3249–3252.

(17) Heurlin, M.; Wickert, P.; Fält, S.; Borgström, M. T.; Deppert, K.; Samuelson, L.; Magnusson, M. H. Axial InP nanowire tandem junction grown on a silicon substrate. *Nano Lett.* **2011**, *11*, 2028–2031.

(18) Huang, N.; Lin, C.; Povinelli, M. L. Broadband absorption of semiconductor nanowire arrays for photovoltaic applications. *J. Opt.* **2012**, *14*, 024004.

(19) Madaria, A. R.; Yao, M.; Chi, C.; Huang, N.; Lin, C.; Li, R.; Povinelli, M. L.; Dapkus, P. D.; Zhou, C. Toward optimized light utilization in nanowire arrays using scalable nanosphere lithography and selected area growth. *Nano Lett.* **2012**, *12*, 2839–2845.

(20) Howell, S. L.; Padalkar, S.; Yoon, K.; Li, Q.; Koleske, D. D.; Wierer, J. J.; Wang, G. T.; Lauhon, L. J. Spatial mapping of efficiency of GaN/InGaN nanowire array solar cells using scanning photocurrent microscopy. *Nano Lett.* **2013**, *13*, 5123–5128.

(21) Wallentin, J.; Anttu, N.; Asoli, D.; Huffman, M.; Aberg, I.; Magnusson, M. H.; Siefert, G.; Fuss-Kailuweit, P.; Dimroth, F.; Witzigmann, B.; Xu, H. Q.; Samuelson, L.; Deppert, K.; Borgström, M. T. InP nanowire array solar cells achieving 13.8% efficiency by exceeding the ray optics limit. *Science* **2013**, *339*, 1057–1060.

(22) Bermel, P. Photon management modeling and beyond for photovoltaics. *Opt. Commun.* **2014**, *314*, 66–70.

(23) LaPierre, R. R.; Chia, A. C. E.; Gibson, S. J.; Haapamaki, C. M.; Boulanger, J.; Yee, R.; Kuyanov, P.; Zhang, J.; Tajik, N.; Jewell, N.; Rahman, K. M. A. Nanowire photovoltaics: review of design for high efficiency. *Phys. Status Solidi* **2013**, *16*, III–V.

(24) Kailuweit, P.; Peters, M.; Leene, J.; Mergenthaler, K.; Dimroth, F.; Bett, A. W. Numerical simulations of absorption properties of InP nanowires for solar cell applications. *Prog. Photovolt. Res. Appl.* **2011**, *20*, 945–953.

(25) Li, J.; Yu, H.; Li, Y. Solar energy harnessing in hexagonally arranged Si nanowire arrays and effects of array symmetry on optical characteristics. *Nanotechnology* **2012**, *23*, 194010.

(26) Yu, Z.; Raman, A.; Fan, S. Nanophotonic light-trapping theory for solar cells. *Appl. Phys. A: Mater. Sci. Process.* **2011**, *105*, 329–339.

(27) Anttu, N.; Xu, H. Q. Coupling of light into nanowire arrays and subsequent absorption. *J. Nanosci. Nanotechnol.* **2010**, *10*, 7183–7187.

(28) Anttu, N.; Xu, H. Q. Efficient light management in vertical nanowire arrays for photovoltaics. *Opt. Express* **2013**, *21*, 27589–27605.

(29) ASTM. *Reference Solar Spectral Irradiance: Air Mass 1.5 Spectra*. <http://rredc.nrel.gov/solar/spectra/am1.5>.

(30) Hutchinson, N. J.; Coquil, T.; Navid, A.; Pilon, L. Effective optical properties of highly ordered mesoporous thin films. *Thin Solid Films* **2010**, *518*, 2141–2146.

(31) Navid, A.; Pilon, L. Effect of polarization and morphology on the optical properties of absorbing nanoporous thin films. *Thin Solid Films* **2008**, *516*, 4159–4167.

(32) Bruggeman, D. A. G. Berechnung verschiedener physikalischer konstanten von heterogenen substanzen. *Ann. Phys.* **1935**, *416*, 636–664.

(33) del Rio, J. A.; Whitaker, S. Maxwell's equations in two-phase systems I: local electrodynamic equilibrium. *Transport Porous Med.* **2000**, *39*, 159–186.

(34) del Rio, J. A.; Whitaker, S. Maxwell's equations in two-phase systems II: two-equation model. *Transport Porous Med.* **2000**, *39*, 259–287.

(35) Keavney, C.; Haven, V.; Vernon, S. Emitter structures in MOCVD InP solar cells. *Conf. Rec., 21st IEEE Photovoltaic Spec. Conf.* **1990**, 141–144.

(36) Green, M. A.; Emery, K.; Hishikawa, Y.; Warta, W.; Dunlop, E. D. Solar cell efficiency tables (version 39). *Prog. Photovoltaic Res. Appl.* **2012**, *20*, 12–20.

(37) Dossou, K. B.; Botten, L. C.; Asatryan, A. A.; Sturmberg, B. C. P.; Byrne, M. A.; Poulton, C. G.; McPhedran, R. C.; de Sterke, C. M. Modal formulation for diffraction by absorbing photonic crystal slabs. *J. Opt. Soc. Am. A* **2012**, *29*, 817–831.

(38) EMUstack: open-source simulation package; emustack.com.